PHOTONICS Research

Antibunching and superbunching photon correlations in pseudo-natural light

ZHIYUAN YE,[1] HAI-BO WANG,[1] JUN XIONG,[1,2] AND KAIGE WANG[1,3]

[1]*Department of Physics, Applied Optics Beijing Area Major Laboratory, Beijing Normal University, Beijing 100875, China*
[2]*e-mail: junxiong@bnu.edu.cn*
[3]*e-mail: wangkg@bnu.edu.cn*

Since Hanbury Brown and Twiss revealed the photon bunching effect of a thermal light source in 1956, almost all studies in correlation optics have been based on light's intensity fluctuation, regardless of fact that the polarization fluctuation is a basic attribute of natural light. In this work, we uncover the veil of the polarization fluctuation and corresponding photon correlations by proposing a new light source model, termed pseudo-natural light, embodying both intensity and polarization fluctuations. Unexpectedly, the strong antibunching and superbunching effects can be simultaneously realized in such a new source, whose second-order correlation coefficient $g^{(2)}$ can be continuously modulated across 1. For the symmetric Bernoulli distribution of the polarization fluctuation, particularly, $g^{(2)}$ can be in principle from 0 to unlimitedly large. In pseudo-natural light, while the bunching effects of both intensity and polarization fluctuations enhance the bunching to superbunching photon correlation, the antibunching correlation of the polarization fluctuation can also be extracted through the procedure of division operation in the experiment. The antibunching effect and the combination with the bunching one will arouse new applications in quantum imaging. As heuristic examples, we carry out high-quality positive or negative ghost imaging, and devise high-efficiency polarization-sensitive and edge-enhanced imaging. This work, therefore, sheds light on the development of multiple and broad correlation functions for natural light. © 2022 Chinese Laser Press

https://doi.org/10.1364/PRJ.446935

1. INTRODUCTION

In 1956, Hanbury Brown and Twiss (HBT) [1,2] proposed an intensity interferometer to measure the angular diameter of a star. The star light as natural light obeys the photon statistics of a thermal light field, i.e., the bunching correlation for bosons, where the second-order correlation coefficient $g^{(2)}$ of the optical field follows $1 < g^{(2)} \leq 2$. The photon bunching in intensity correlation affords the coherence information of remote star light in an HBT intensity interferometer. Since the beginning of this century, the bunching correlation in thermal light has had many applications in a nonlocal imaging technique, such as ghost imaging (GI), ghost interference, and subwavelength interference [3–15]. Especially, the GI technique has made widespread attention and revolutionary progress in the past decade. In these applications, most experiments employ the pseudo-thermal light source [16], which has a similar statistical correlation to the true thermal light but possesses a very slow temporal response.

Due to the Pauli exclusive principle and Fermi–Dirac statistics, fermions in a thermal source can manifest antibunching effect with $0 \leq g^{(2)} < 1$ [17–19]. Gan *et al.* [20] proposed a scheme of magnifying GI of an electron microscope and

pointed out that quantum imaging with thermal fermions can construct dark patterns against a bright intensity background. The dark image (or negative image) by antibunching correlation may increase the visibility perfectly against the maximum visibility of one-third for the positive GI by the bunching correlation of thermal photons. As for photons, however, the antibunching phenomenon is usually regarded as a signature of nonclassical light [21–23], such as the photon number state. This distinguishing feature highlights the quantum nature of fermions without classical analog. It is worth noting that the classical anticorrelation phenomena can occur between reflected and transmitted speckle patterns from opaque disordered media [24,25], but the antibunching effect is very weak. On the other hand, the photon superbunching effect is meant for $g^{(2)} > 2$, and it can also improve the visibility and resolution of GI. This effect can be carried out by nonlinear interaction between light and atoms [26–29]. Recently, some simple and practical superbunching schemes for classical light were reported and can be applied to GI in the temporal domain [30] or in the spatial domain [31,32], and notably, these effects in classical regimes can be well interpreted by means of the speckle's non-Rayleigh statistics [33–35] in either

the temporal or spatial domain. Also, some schemes have been proposed to generate a $g^{(2)}$-switchable light source in the temporal domain [36] or in the spatial domain from coherent to thermal [37], from subthermal to superthermal [38], and controllable superthermal [39].

In conventional optical imaging, the most popular light sources come from natural sunlight. When sunlight is applied to GI, the main obstacle is its fast temporal fluctuation in the face of present, relatively slower response detectors. Liu *et al.* [40] performed the first experiment with lensless GI with sunlight, taking a step toward the practical application of natural light in GI. Natural light might contain both intensity fluctuation (IF) and polarization fluctuation (PF) [41], and several interesting models for the generalized HBT effect [42–46] with a random vector field have been proposed. To our knowledge, however, most studies in correlation optics and imaging applications are based on light's IF regardless of PF. In this work, we propose a simple scheme to exploit both antibunching and superbunching effects for PF in classical light. For the symmetric Bernoulli distribution of PF in coherent light, the spectrum of $g^{(2)}$ can be considerably broad, from zero for antibunching and unlimitedly large for superbunching. Similar to pseudo-thermal light, we introduce a pseudo-natural light source in which polarized pseudo-thermal light passes through a liquid crystal spatial light modulator (SLM) [47,48] to acquire independent IF and PF with much slower coherence time in comparison with polarization time of natural light [49]. In the pseudo-natural light model, the positive correlations of the IF and PF can be enhanced with each other to supercorrelation. However, the anticorrelation of PF can be extracted from the mixed correlations of PF and IF. Using the pseudo-natural light source, we perform high-quality positive and negative GI and carry out other relevant applications in the experiments.

2. THEORY

Considering a polarized beam of intensity I_S passing through a polarizing beam splitter (PBS), as shown in Fig. 1(a), the intensities of two outgoing beams are given by $I_x = pI_S$ and $I_y = (1 - p)I_S$, where $p \in [0,1]$ is a parameter related to the polarization state of the input beam. When input beam has the PF, p becomes a random variable. We first consider the case when the input intensity I_S is fixed, such as a laser beam. Due to the PF of the input beam, the two outgoing beams from PBS have the IF with $g_{I_x}^{(2)} = g_p^{(2)} = 1 + \sigma_p^2/\mu_p^2$ and $g_{I_y}^{(2)} = g_{1-p}^{(2)} = 1 + \sigma_p^2/(1 - \mu_p)^2$, where we define $g_I^{(2)} = \langle I^2 \rangle / \langle I \rangle^2 = 1 + \sigma_I^2/\mu_I^2$ with the mean value $\mu_I = \langle I \rangle$ and variance $\sigma_I^2 = \langle I^2 \rangle - \langle I \rangle^2$ for the random variable I. However, the cross-correlation function between the two outgoing beams is given by

$$g_{I_x I_y}^{(2)} = \frac{\langle I_x I_y \rangle}{\langle I_x \rangle \langle I_y \rangle} = g_{p(1-p)}^{(2)} = 1 - \frac{\sigma_p^2}{\mu_p(1 - \mu_p)}. \quad \text{(1)}$$

Since $0 \le g_{p(1-p)}^{(2)} < 1$, the intensity-stable beam with the PF possesses the antibunching effect. When the horizontal and vertical polarization components balance out in the PF, i.e., $\mu_p = 1/2$, we get $g_p^{(2)} = g_{1-p}^{(2)}$ and $g_p^{(2)} + g_{p(1-p)}^{(2)} = 2$.
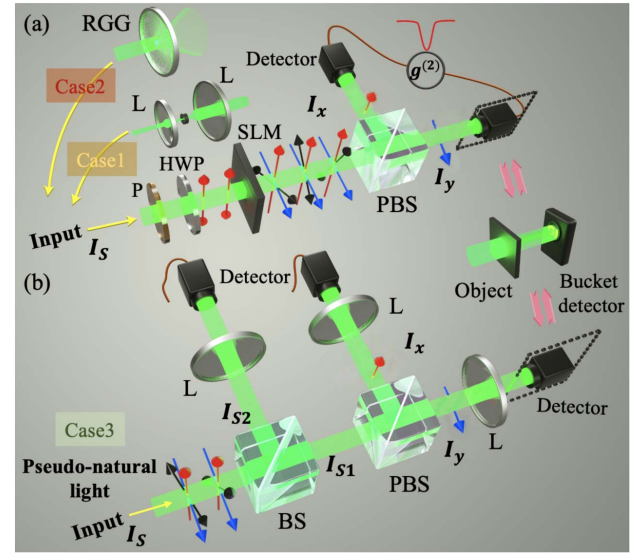

Fig. 1. (a) Schematic diagram of the PBS model: two CMOS-based image sensors (detectors) for recording intensity correlation. When the detector in the black-dotted box is replaced with an object and a bucket detector, the setup can facilitate GI experiments. A programmable SLM is utilized to generate the PF of the wavefront with adjustable coherence time. A 4-f lens system (not shown) is used to image the SLM plane onto the detection plane. (b) Schematic diagram of GI for pseudo-natural light: an ordinary BS is introduced to obtain additional reference beam for division and subtraction operations. P, linear polarizer; HWP, half-wave plate; L, lens; RGG, rotating ground glass.

To be clear, we show two examples. (i) Random linearly polarized light with polarization angle θ, which is uniformly distributed in $[0, \pi]$. We have $p = \cos^2 \theta$, $\mu_p = 1/2$, $\langle p^2 \rangle = 3/8$, $\sigma_p^2 = 1/8$, and obtain $g_p^{(2)} = g_{1-p}^{(2)} = 3/2$ and $g_{p(1-p)}^{(2)} = 1/2$. (ii) Linearly polarized light with only two polarization angles, i.e., a Bernoulli distribution. The probability function for random variable p is $P(p) = \begin{cases} c, p = p_1 \\ 1 - c, p = p_2 \end{cases}$, where $0 < c < 1$ and $p_1 \ne p_2$. We can calculate $\mu_p = p_1 c + p_2(1 - c)$, $\langle p^2 \rangle = p_1^2 c + p_2^2(1 - c)$, $\sigma_p^2 = c(1 - c)(p_1 - p_2)^2$, and accordingly, $g_p^{(2)}, g_{1-p}^{(2)}$, and $g_{p(1-p)}^{(2)}$. For example, in the symmetric configuration of $p_1 + p_2 = 1$, we have $\mu_p = p_1 c + (1 - p_1)(1 - c)$ and $\sigma_p^2 = c(1 - c)(2p_1 - 1)^2$. Especially if the beam contains only horizontal and vertical polarization states, we obtain $g_p^{(2)} = 1/c$, $g_{1-p}^{(2)} = 1/(1 - c)$, and $g_{p(1-p)}^{(2)} = 0$. The minimum antibunching effect is realized, since in this case every photon chooses only one way in the PBS with certainty. However, the maximum superbunching effect ($g_p^{(2)}$ or $g_{1-p}^{(2)}$) can be unlimitedly large as c is close to 0 or 1.

A general polarization state of monochromatic plane wave can be described by the Stokes vector on the Poincaré sphere [50],

$$\begin{pmatrix} S_0 \\ S_1 \\ S_2 \\ S_3 \end{pmatrix} = I_S \begin{pmatrix} 1 \\ \cos(2\chi)\cos(2\psi) \\ \cos(2\chi)\sin(2\psi) \\ \sin(2\chi) \end{pmatrix}, \quad \text{(2)}$$

where ψ $(0 \leq \psi \leq \pi)$ specifies the orientation and χ $(-\pi/4 \leq \chi \leq \pi/4)$ characterizes the ellipticity of the polarization ellipse, while 2χ and 2ψ stand for the spherical angular coordinates of latitude and longitude, respectively. When the intensity of a plane wave is given, $S_0 = I_S$; thus, it has defined the radius of the Poincaré sphere. The probability function $P(2\chi, 2\psi)$ on the Poincaré sphere can describe the PF. Because of $S_1 = I_x - I_y = (2p - 1)I_S$, it has $p = (\cos 2\chi \cos 2\psi + 1)/2$. As a result, we can calculate $\langle p \rangle$, $\langle p^2 \rangle$ on the Poincaré sphere, and the corresponding second-order correlation functions. For example, for the uniform probability distribution on the Poincaré sphere $P(2\chi, 2\psi) = 1/4\pi$, we have $\mu_p = 1/2$, $\sigma_p^2 = 1/12$, $g_p^{(2)} = g_{1-p}^{(2)} = 4/3$, and $g_{p(1-p)}^{(2)} = 2/3$. Both bunching and antibunching effects coexist, and $g_p^{(2)} + g_{p(1-p)}^{(2)} = 2$. As for the case of random circularly polarized light, which has only left-handed and right-handed states (the north pole and south pole on the Poincaré sphere), the IF will not exist after passing through a PBS. To gain the IF, however, one can introduce a quarter-wave plate in front of the PBS.

We now consider the case in which the beam of intensity I_S contains both IF and PF, which are independent of each other, possibly similar to some of natural light. When the beam impinges on a PBS, three second-order correlation coefficients of two outgoing beams are obtained to be

$$
\begin{aligned}
g_{I_x}^{(2)} &= g_{I_S}^{(2)} g_p^{(2)}, \\
g_{I_y}^{(2)} &= g_{I_S}^{(2)} g_{1-p}^{(2)}, \\
g_{I_x I_y}^{(2)} &= g_{I_S}^{(2)} g_{p(1-p)}^{(2)}.
\end{aligned}
\tag{3}
$$

The intensity correlation functions of outgoing beams from the PBS can be factorized according to independent IF and PF. Since $g_{I_S}^{(2)}$, $g_p^{(2)}$, and $g_{1-p}^{(2)}$ are positive correlation functions $(g^{(2)} > 1)$, $g_{I_x}^{(2)}$ and $g_{I_y}^{(2)}$ are also positive correlation ones, possibly superbunching. However, $g_{p(1-p)}^{(2)}$ is an anticorrelation one $(g^{(2)} < 1)$, so the cross-intensity correlation $g_{I_x I_y}^{(2)}$ may be positive or anticorrelation, depending on the competition between two opposite correlations. Hence, in the PBS scheme, the IF of the input beam enhances the positive correlation of each polarization mode while counteracting the anticorrelation between two polarization modes. It would be an obstacle to gain the antibunching effect for natural light.

To surpass the obstacle, we propose a scheme of combination of a beam splitter (BS) and a PBS in Fig. 1(b). The pseudo-natural light is divided into two parts after the BS with the intensities $I_{S1} = tI_S$ and $I_{S2} = rI_S$, where t and r are the transmissivity and the reflectivity of the BS, respectively. After the PBS, the intensities of the two outgoing beams for the horizontal and vertical polarization modes are written as $I_x = pI_{S1} = ptI_S$ and $I_y = (1 - p)I_{S1} = (1 - p)tI_S$. It is clear that the second-order correlation functions of I_x and I_y follow Eq. (3) because of $g_{I_{S1}}^{(2)} = g_{I_S}^{(2)}$.

We now perform some basic operations between the random variables I_{S2} and I_x (I_y). First, we define the division operations $p_x \equiv I_x/I_{S2} = (t/r)p$ and $p_y \equiv I_y/I_{S2} = (t/r)(1 - p)$,

so the random intensity of the carrier beam has been eliminated. Thus we obtain

$$
\begin{aligned}
g_{p_x I_x}^{(2)} &= g_{p_x}^{(2)} = g_p^{(2)}, \\
g_{p_y I_y}^{(2)} &= g_{p_y}^{(2)} = g_{1-p}^{(2)}, \\
g_{p_x I_y}^{(2)} &= g_{I_x p_y}^{(2)} = g_{p_x p_y}^{(2)} = g_{p(1-p)}^{(2)}.
\end{aligned}
\tag{4}
$$

As a result, all the correlation functions related to the PF only have been extracted. Second, we introduce the subtraction operations $I_{S2} - I_x = (r - pt)I_S$ and $I_{S2} - I_y = [r - (1 - p)t]I_S$, and calculate the cross-correlation functions,

$$
\begin{aligned}
g_{(I_{S2} - I_x)I_y}^{(2)} &= \frac{(1 - 2t)(1 - \langle p \rangle) + t\langle (1 - p)^2 \rangle}{(1 - 2t)(1 - \langle p \rangle) + t\langle (1 - p) \rangle^2} g_{I_S}^{(2)}, \\
g_{(I_{S2} - I_y)I_x}^{(2)} &= \frac{(1 - 2t)\langle p \rangle + t\langle p^2 \rangle}{(1 - 2t)\langle p \rangle + t\langle p \rangle^2} g_{I_S}^{(2)},
\end{aligned}
\tag{5}
$$

where the lossless BS condition $r + t = 1$ has been applied. For a balanced lossless BS, we arrive at

$$
g_{(I_{S2} - I_x)I_y}^{(2)} = g_{1-p}^{(2)} g_{I_S}^{(2)}, \qquad g_{(I_{S2} - I_y)I_x}^{(2)} = g_p^{(2)} g_{I_S}^{(2)}.
\tag{6}
$$

The results are exactly the same as the first two equations in Eq. (3), but here the cross-correlations of two polarization modes replace the autocorrelations of each polarization mode. Since two correlated beams are ready, the present method is convenient for GI performance.

3. RESULTS

A. Experimental Observations of Antibunching and Superbunching

In the experimental performance, we discuss three cases for the PF of the Bernoulli distribution with the symmetrical polarization configuration $p_1 + p_2 = 1$ (see the experimental calibration of the SLM in Appendix A.1). In Case 1 and Case 2, coherent light and pseudo-thermal light drive the SLM, respectively; then these beams are injected onto a PBS, shown in Fig. 1(a). In Case 3, however, pseudo-thermal light drives the SLM to form pseudo-natural light with independent IF and PF as Case 2; then pseudo-natural light impinges on a BS and follows the PBS, shown in Fig. 1(b). We measure the second-order correlation coefficients as functions of p_1 and c in Fig. 2.

For Case 1, when the coherent light drives the SLM, we can observe $g_p^{(2)}$, $g_{1-p}^{(2)}$, and $g_{p(1-p)}^{(2)}$ of PF directly in Figs. 2(a1) and 2(a2). In Fig. 2(a1) [also Figs. 2(b1) and 2(c1)], the probability of two polarization modes is balanced as $c = 1/2$. The experimental results demonstrate the positive correlation $g_p^{(2)} = g_{1-p}^{(2)} > 1$ and anticorrelation $g_{p(1-p)}^{(2)} < 1$ (from 0.25 to 0.99), approximately satisfying $g_p^{(2)} + g_{p(1-p)}^{(2)} = 2$. In Fig. 2(a2) [also Figs. 2(b2) and 2(c2)], the maximum linear polarization parameter $p_1 = 0.94$ in the SLM is taken; then we have the minimum anticorrelation $g_{p(1-p)}^{(2)} = 0.25 \pm 0.03$ at $c = 1/2$. However, larger positive correlation coefficients (superbunching effect) for each outgoing polarization mode $g_p^{(2)} = 5 \pm 0.6$ and $g_{1-p}^{(2)} = 4.3 \pm 0.5$ are generated for $c = 0.94$ and 0.06, respectively.

For Case 2 we measure $g_{I_x}^{(2)}$, $g_{I_y}^{(2)}$, and $g_{I_x I_y}^{(2)}$ for pseudo-natural light in Figs. 2(b1) and 2(b2). These second-order
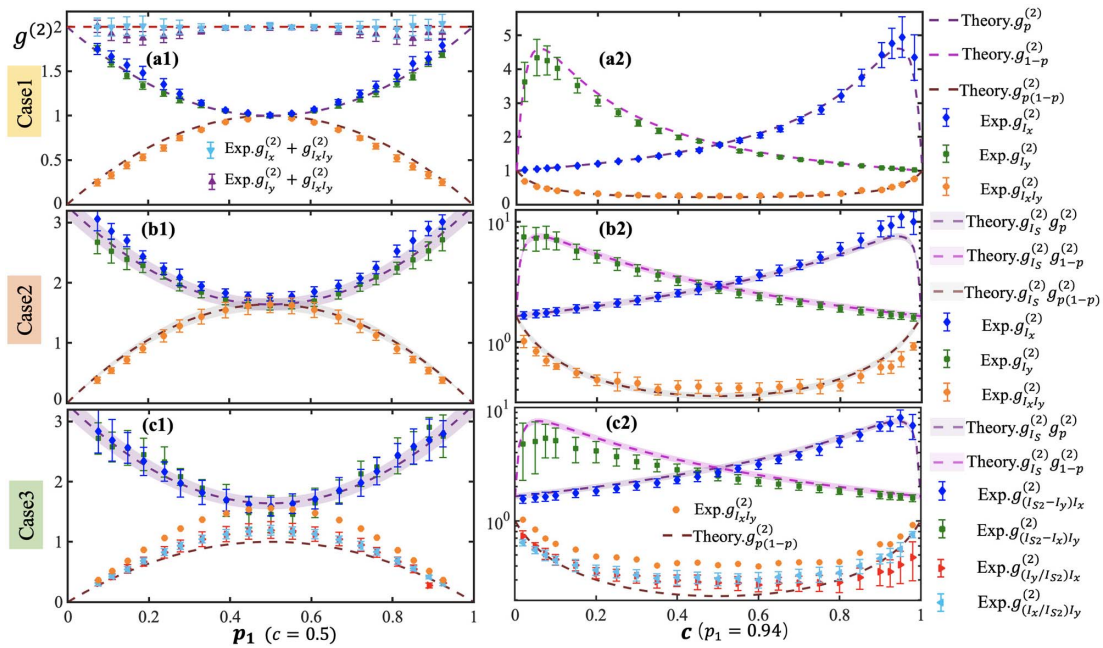
Fig. 2. Second-order correlation coefficients as functions of p_1 and c for the symmetric Bernoulli distribution of PF. Case 1, coherent light with PF. (a1) Antibunching and bunching effects are exhibited in cross- and autocorrelation coefficients satisfying $g_p^{(2)} + g_{p(1-p)}^{(2)} \approx 2$; (a2) superbunching and antibunching effects can be observed with some values of c. Case 2 and Case 3, pseudo-thermal light with PF. (b1) and (b2) With the introduction of a statistically independent IF source, i.e., pseudo-thermal light, all the second-order correlation coefficients are multiplied by the second-order correlation coefficients of $g_{I_S}^{(2)}$, such that the superbunching is enhanced but the antibunching is weakened or even disappears. As a result, the cross-correlation coefficient of pseudo-thermal light is neither too high nor too low. To overcome this obstacle, division and subtraction are performed to gain anticorrelation and supercorrelation in (c1) and (c2) according to setup of Fig. 1(b). Note that (a1), (b1), and (c1) share the same abscissa with c fixed as 0.5, while (a2), (b2), and (c2) share the same abscissa with p_1 fixed as 0.94. Also see the experimental calibration of the SLM in Appendix A.1.

correlation coefficients are similar to $g_p^{(2)}$, $g_{1-p}^{(2)}$, and $g_{p(1-p)}^{(2)}$ in Figs. 2(a1) and 2(a2) but enhanced by $g_{I_S}^{(2)} = 1.6 \pm 0.1$ due to Eq. (3). As a result, the enhanced superbunching effect can be observed with the maximum values of 10.3 and 8.1 at $c = 0.94$ and 0.06, respectively. However, the cross-correlation coefficient $g_{I_x I_y}^{(2)}$ varies from 0.38 to 1.64 in Fig. 2(b1), i.e., from anticorrelation to positive correlation, against the whole anti-correlation in Case 1.

For Case 3, by combination of an ordinary BS and a PBS in Fig. 1(b), we perform the division operation and subtraction operation mentioned above to obtain the original antibunching correlation of PF and superbunching correlation of both IF and PF, respectively. By the division operation, $g_{p_x I_y}^{(2)}$ and $g_{I_x p_y}^{(2)}$ are measured in the range of 0.31–1.21 with respect to the range of 0.38–1.64 for $g_{I_x I_y}^{(2)}$ [see lower part in Fig. 2(c1)]. Since very small intensities will give incorrect results, these records have to be deleted in the division. For this reason, the IF is partly eliminated. As seen in Fig. 2(c2), by the subtraction operation the superbunching effect can be realized with the maximum records of 8.3 and 6.0 at $c = 0.94$ and 0.08, respectively.

In the experiment, the values of p are limited by the SLM and PBS in the range [0.06, 0.94] (see Appendix A.1 for the experimental calibration of the SLM and error analysis). So, we can observe the second-order correlation coefficients ranging from a minimum of 0.25 to a maximum of 10.3. Hence, this simple setup can be viewed as a special light source with tunable photon correlation from antibunching to superbunching.

B. Positive and Negative Ghost Images

Next, we observe HBT curves and perform GI experiments. As shown in Fig. 1, the detector in the dotted box is replaced with an object and a bucket detector. The experimental results are presented in Figs. 3 and 4. We first consider the PF source driven by coherent light. For the symmetric Bernoulli distribution ($p_1 = 0.94$, $c = 0.5$) and uniform distribution of PF, the antibunching HBT curves with the minimum $g_{I_x I_y}^{(2)} = 0.26$ and 0.54 are plotted in Figs. 3(a1) and 3(a2), respectively. As a result, we observe dark ghost images in Figs. 3(b1) and 3(b2) with much better contrast-to-noise ratio (CNR, also see Eqs. (A2) and (A3) in Appendix A.4) [51].

In Fig. 4, pseudo-natural light is formed with the symmetric Bernoulli distribution of PF driven by pseudo-thermal light. We consider two cases: ($p_1 = 0.94$, $c = 0.94$) in Figs. 4(a1) and 4(b1) and ($p_1 = 0.94$, $c = 0.5$) in Figs. 4(a2) and 4(b2). For the former, we perform the subtraction operation and observe the significant superbunching effect ($g^{(2)} = 8.43$). As for the latter, we perform the division operation and extract the antibunching effect of PF ($g^{(2)} = 0.32$). Hence the corresponding positive image in Fig. 4(b1) and negative image in Fig. 4(b2) have much better CNRs.

C. Polarization-Sensitive GI

The combination of two opposite photon correlations can find a variety of applications. Here we demonstrate polarization-sensitive imaging as getting started, which is developed to
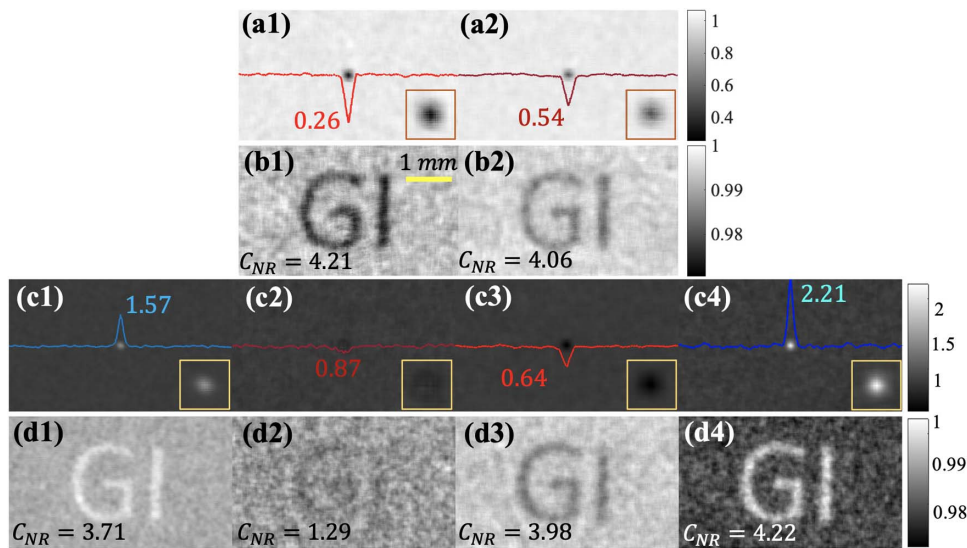
Fig. 3. HBT curves of bunching and antibunching effects and corresponding GIs for different fluctuation sources. (a1) and (b1) Symmetric Bernoulli distribution of PF ($p_1 = 0.94$, $c = 0.5$); (a2) and (b2) uniform distribution of PF; (c1) and (d1) linearly polarized pseudo-thermal light of IF; (c2)–(c4) and (d2)–(d4) pseudo-natural light with both IF and PF (uniform distribution), where, in (c3) and (d3) division is performed, and in (c4) and (d4) subtraction is performed. 3000 shots contribute to each image, and scale bar is 1 mm, similarly hereinafter.
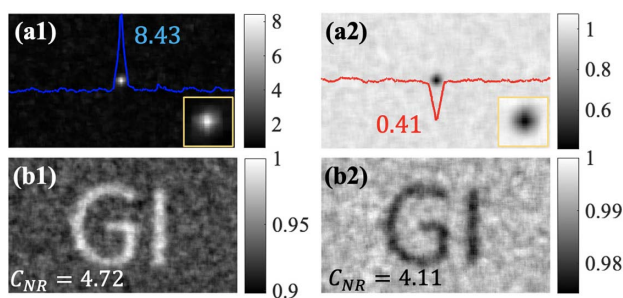

Fig. 4. Same as Fig. 3. The sources are pseudo-natural light with both IF and PF (symmetric Bernoulli distribution), where, in (a1) and (b1) $p_1 = 0.94$, $c = 0.94$, subtraction is performed; in (a2) and (b2) $p_1 = 0.94$, $c = 0.5$, division is performed.

Fig. 5. (a) Schematic diagram of GI with polarization identification. (b1) Positive image with I_A only; (b2) negative image with I_B only; (b3) polarization-sensitive image with both I_A and I_B. See Appendix A.3 for more experimental details.

enhance the visibility of targets in scattering media [52]. As shown in Fig. 5(a), I_A and I_B are intensities of two independent light sources A and B with IF and PF, respectively. Beam A is linearly polarized with a solid angle oriented at 45°. Two beams are mixed in a PBS to generate a hybrid illumination. The targets are now polarized—two letters have orthogonal polarization. When source B (A) is turned off, the positive (negative) image appears for the horizontally (vertically) polarized letter, as shown in Fig. 5(b1) [Fig. 5(b2)], which is also illustrated by the inset table in Fig. 5(a). For the hybrid illumination, however, two letters appear simultaneously and identifiably in Fig. 5(b3) with diametrically opposite intensity below and above the background. This feature is superior to the common scheme of polarization-sensitive imaging. Also see Appendix A.3 for more experimental details. It is worth noting that the present scheme can achieve resolution-enhanced measurement of polarization-sensitive phase objects, just like the recent work on polarization
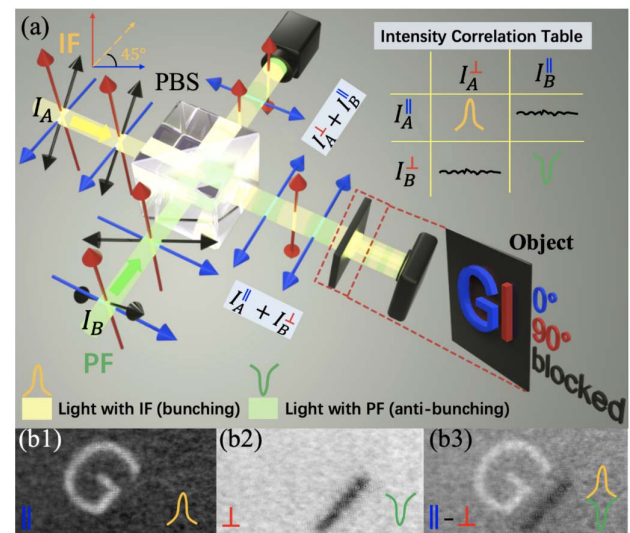
entanglement-enabled quantum holography, proposed by Defienne *et al.* [53].

D. Customization of the Spatial Pattern of Second-Order Correlation Functions

In general, the combination of classical spatial antibunching and bunching effects also provides an alternative toolbox for the customization of the second-order correlation functions. For example, the second-order correlation coefficient can be continuously adjustable in a wide range across 1, which has been shown in Fig. 2. Also, the spatial structure of the
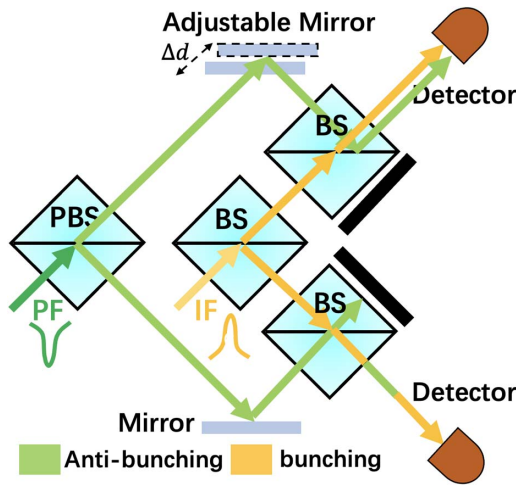
Fig. 6. Schematic diagram of the customization of second-order correlation functions. Similar to Fig. 5, two independent fluctuation sources are combined. The difference is that an asymmetric offset is introduced in the PF path, which can be achieved by adjusting the angle of a mirror.

second-order correlation function can be tailored based on the opposite spatial correlation distributions.

The schematic diagram of the second example is shown in Fig. 6, which is very similar to Fig. 5(a), but the two beams corresponding to independent IF and PF sources are offset by an adjustable mirror. Figure 7(a) shows the simulation object (256 × 256 pixels). The size of the speckle unit, i.e., the half-height width of the second-order correlation function, is set to ~6 pixels. First, we introduce the customization of a hollow-like pattern of the second-order correlation function shown in

Fig. 7(b1): no offset, but the size of the speckle unit of the IF source is increased to ~9 pixels. As a result, the central area of the second-order correlation function is about 1, while the surrounding region is larger than 1, and a fuzzy positive image is shown in Fig. 7(c1).

Then we introduce the offset of six pixels between the two beams. Two spots with a peak and a dip in the second-order correlation functions are formed with different directions [Figs. 7(b2)–7(b4)] by adjusting the angle of the mirror. With these tailored second-order correlation functions, we can observe the various reconstructed images [Figs. 7(c2)–7(c4)] with edges enhanced at corresponding directions. For comparisons of edge quality, Figs. 7(d1)–7(d4) show one-dimensional (1D) profiles of images in the direction of the corresponding arrow. Hence, the introduction of PF has expanded more unexpected possibilities for GI applications.

4. CONCLUSION

In summary, we have demonstrated antibunching and superbunching effects in the PF of classical light and applied them to high-quality positive and negative GI, and proposed two application examples. Usually either the superbunching effect or the anti-bunching effect can be found in some quantum optical systems. Our model is completely limited in the scope of classical optics but covers both superbunching and antibunching effects. The present scheme is very simple and significantly effective for a special light source with a multiple and broad correlation property. At present, however, while pseudo-thermal light with IF only is still the most popular source in correlation optics, our work affords an alternative choice with enhancements. Sunlight offers humans a visible world free of charge. As natural sunlight contains both IF and PF, our work also opens the way for wide applications for natural light.
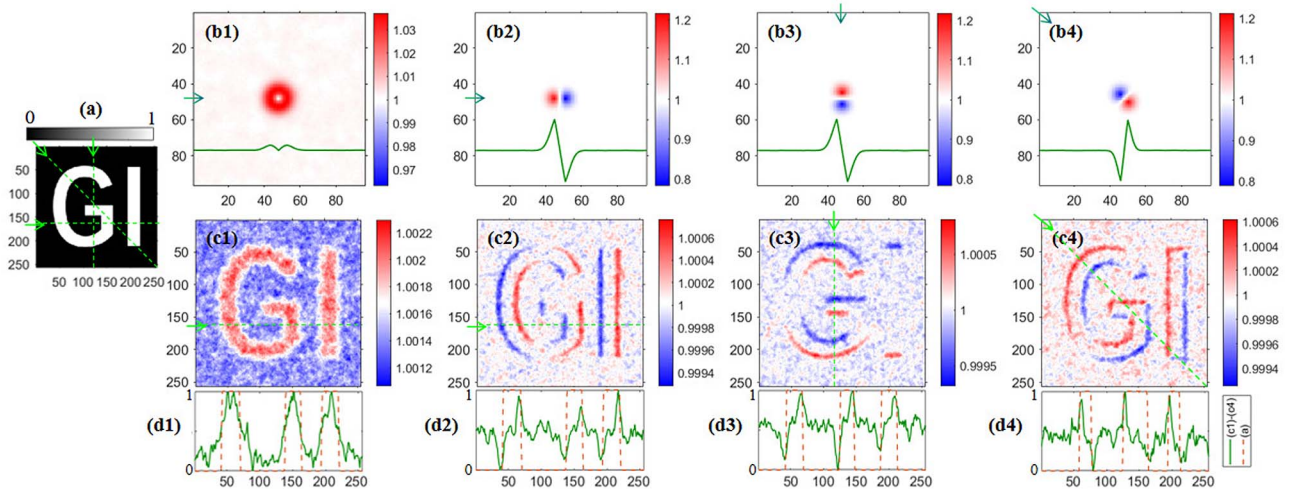

Fig. 7. Customization of various unique second-order correlation functions or point spread functions of the GI system. (a) Simulation object; (b1) hollow-like pattern; and (b2)–(b4) peak dip-like patterns with different directions by changing the angle of the mirror in Fig. 6. Note that only the middle area (96 × 96 pixels) is displayed in (b1)–(b4), where green lines are 1D distributions with the directions indicated by corresponding green arrows. (c1)–(c4) Simulation imaging results corresponding to different point spread functions; 500,000 shots contribute to each image. (d1)–(d4) Corresponding 1D profiles of images with the directions indicated by corresponding green arrows. The horizontal and longitudinal coordinates in (d1)–(d4) are pixel position and normalized intensity, respectively. For comparison, the solid line and the dashed line represent the edge-enhanced image and the original one, respectively.

APPENDIX A

1. Experimental Calibration of the SLM

The coherent beam in this experiment comes from a continuous semiconductor laser (Laserwave, LWGL532 160105) with a center wavelength of 532 nm, and the actual optical power is approximately 160 mW. A transmissive SLM (Daheng Optics, GCI-77) is utilized to generate the PF, so we can artificially preload the profile on the SLM to modulate the polarization distribution of the wavefront. The coherence time of the PFs of this light source is slow enough such that we can easily observe the antibunching effect with CMOS-based detectors (Sony, IMX226; DAHENG IMAGING, MER-133-54U3M), whose detecting signal-to-noise ratio is 37.79 dB and quantum efficiency is ~64% at 532 nm. The maximum resolution of the profile loaded on the SLM is 768×1024 pixels with the pixel size of 26 μm, and the value range of the parameter k of each pixel unit is [0, 1], which directly modulates the phase and polarization of the wavefront simultaneously. To avoid the influence of the wavefront phase fluctuation on the IF, an optical 4f system is used to image the SLM plane onto the detection plane. Figure 8 shows the experimental calibration between k and the light intensity of I_x, I_y, and I_S ($I_S = I_x + I_y$) using two photodetectors (Thorlabs, PDA100A2), in which all the pixel values of the SLM are set to k, and different k result in different splitting ratios of the PBS. Then the relationship between k and p can be obtained. The green translucent region in Fig. 8 can be approximately regarded as a symmetrical region (k ranges from 0.34 to 1, while p varies from 0.06 to 0.94), approximately satisfying $p_1 + p_2 = 1$. For the sake of simplicity, the independent variable k is taken in the translucent green area regardless of the setting of the Bernoulli distribution or the uniform distr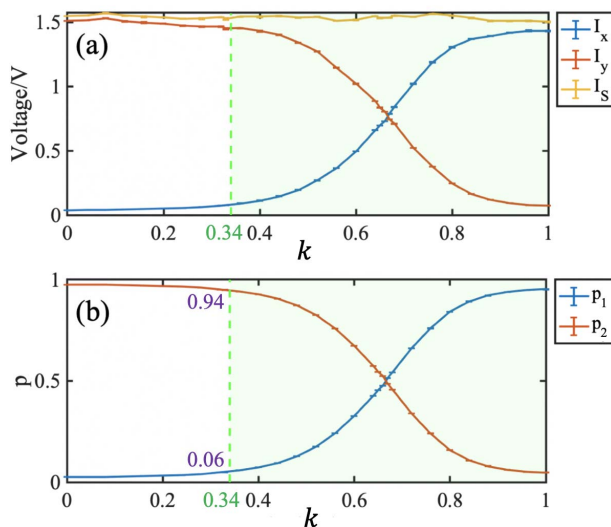ibution. Considering the input light is monochromatic and linearly polarized, this programmable SLM mainly generates a random linearly polarized wavefront modulation with the polarization angle approximately in the range of [16°, 74°] for this selected symmetrical region. Also, the asymmetry of $g_p^{(2)}$ and $g_{1-p}^{(2)}$ in Fig. 8 is mainly caused by the asymmetry of I_x (p_1) and I_y (p_2). In the second-order correlation coefficient measurements (corresponding to Fig. 2), we combine 32×32 pixels into an independent unit, whose parameter k obeys a certain statistical distribution, while in GI experiments (corresponding to Figs. 3–5), we set the size of a single unit to be 7×7 pixels, which determines the spatial resolution. The CMOS-based detector only reads out total light intensity functions as well as the bucket detector in the GI experiments. Whether in the second-order correlation coefficient measurement or in the GI experiments, only 3000 shots are applied.

The theory emphasizes that the theoretical ideal value of the antibunching effect under this PBS model can reach 0, but the lowest value measured by the experiment is only 0.25 since p cannot take all values in [0,1]. The value of p is limited by the extinction ratio of the PBS, the modulation accuracy and depth of the SLM, and the inevitable dark current and readout noise of the detector. Figure 9(b) plots measurement data with 800 profiles that obey the Bernoulli distribution. As we can see, I_S is not a fixed value at experiment, whereas the input is stable coherent light, which is believed to be caused by the dark current of the CMOS image sensor. Also, the process of the SLM switching between two profiles may sometimes have a much slower response or a failure event, which causes the few data in Fig. 9(b) to significantly deviate from the expected fluctuation range. Besides, the grating structure inside the SLM will also have a negative impact on the measurement. Figures 10(a) and 10(b) show the speckle patterns without and with passing through the SLM. Note that the SLM is not activated at this time, and the 4f system is used. The internal grating structure will be mapped out in the speckle pattern in Fig. 10(b), which will inevitably lead to cross talk between pixel units, especially when higher spatial resolution is required. These factors will comprehensively affect the experimental measurement and might eventually lead to deviations from theory and experiment. In general, one can choose more precise devices to enhance the antibunching effect, even close to 0.
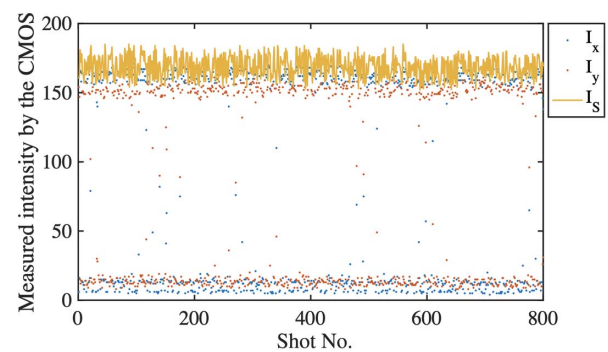
Fig. 8. Experimental calibration of SLM. (a) Relationship between the parameter k loaded on the SLM and the light intensity of I_x, I_y, and I_S ($I_S = I_x + I_y$) using two photodetectors. The green translucent region in (b) can be approximately regarded as a symmetrical region (k ranges from 0.34 to 1 while p varies from 0.06 to 0.94, approximately).

Fig. 9. Raw measurement data of 800 shots that obey the Bernoulli distribution in the second-order correlation coefficient measurement.
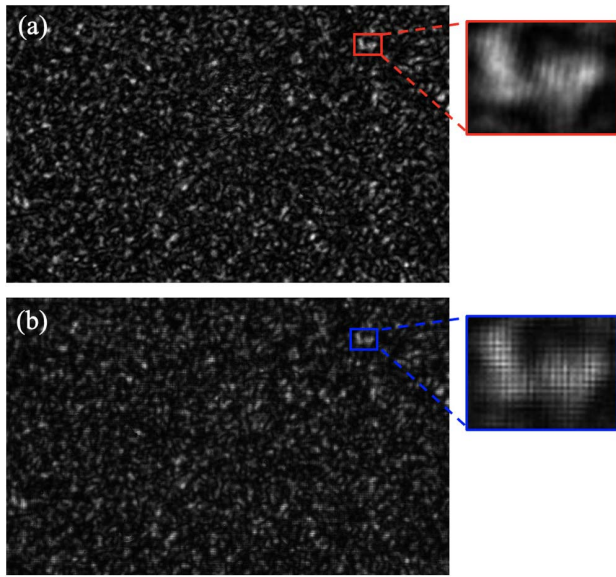
Fig. 10. Raw speckle patterns of pseudo-thermal light. (a) Without and (b) with passing through the SLM.

2. Experimental Details of Pseudo-Natural Light Generation

In the pseudo-natural light model [Case 2 in Fig. 1(a)], the PF is generated by a transmissive SLM experimentally while the IF comes from a pseudo-thermal light source, i.e., a laser beam passes through an unknown rotating ground glass (RGG) disk. Although the statistical correlation or independence [49,54,55] between IF and PF in a genuine natural light source is not clear, the two statistical sources in this work are irrelevant physically. In the imaging system, however, the random speckles do not interfere with each other, and the statistical behavior can be maintained.

In Figs. 2(b1) and 2(b2), we have experimentally verified the strong anticorrelation function, $g_{p(1-p)}^{(2)}$, and the supercorrelation function $g_P^{(2)}$ ($g_{1-p}^{(2)}$) in pseudo-natural light. Admittedly, the superbunching effect realized in the pseudo-natural light can be also viewed as a special case of a type of non-Rayleigh speckle's generation akin to Refs. [30–35]. As evidence, Figures 11(a) and 11(b) show the probability density functions (PDFs) of pseudo-natural light in the spatial domain and temporal domain, respectively, in comparison with standard Rayleigh distribution. Two kinds of pseudo-natural light with uniform distribution and Bernoulli distribution ($p_1 = 0.94$, $c = 0.5$) are taken into account. The experimental results have demonstrated the non-Rayleigh distribution for the superbunching effect in pseudo-natural light, and the spatial and temporal PDFs are very similar.

The intensity contrast of speckles is defined as $C_S = \sqrt{D}/\langle I \rangle$, where D and $\langle I \rangle$ are the speckle's variance and intensity average, respectively. $C_S = 1$ generally stands for Rayleigh speckles. Here, we experimentally measured the intensity contrasts for the pseudo-natural light above. For the pseudo-natural light with linear PF that obeys uniform distribution, we obtain $C_S = 1.10$ and 1.14 for the spatial and temporal domains, respectively; accordingly, for the Bernoulli distribution of two polarization angles ($p_1 = 0.94$, $c = 0.5$), we obtain $C_S = 1.34$ and 1.28. Therefore, the superbunching effect in pseudo-natural light generates non-Rayleigh distribution of speckles.

3. Experimental Details of Polarization-Sensitive GI

The simplified schematic diagram of polarization-sensitive GI is present in Fig. 5(a). Notably, the IF source is not pseudo-thermal light but is generated by an SLM and a polarizer, whose second-order correlation coefficient is identical with $g_p^{(2)}$ or $g_{1-p}^{(2)}$, shown in Section 2. On the other hand, the second-order correlation coefficient of the PF source is the same as $g_{p(1-p)}^{(2)}$. When the two independent sources are incoherently superimposed according to the intensity ratio q, i.e., $q = I_B/I_A$, the second-order correlation function of the mixed illumination can be expressed as

$$g^{(2)} = \frac{g_p^{(2)} + q^2 g_{p(1-p)}^{(2)} + 2q}{(1+q)^2}, \tag{A1}$$

whose value ranges from $g_{p(1-p)}^{(2)}$ (minimum) to $g_p^{(2)}$ (maximum).

Specifically, in the experimental setup in Fig. 12(a), an expanded coherent light is input as the source, and a mask with two rectangular holes divides the expanded coherent light into two separate areas illuminating the SLM. A prism separates the two light fields, and a PBS superimposes the two light fields incoherently. So, it is convenient to adjust the fluctuation characteristics and the unit size of speckle of IF and PF sources.
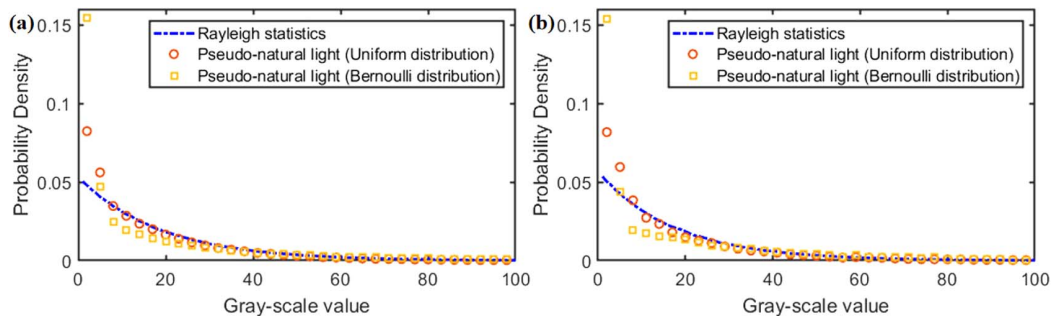

Fig. 11. Probability density distributions of speckles for pseudo-natural light. (a) Spatial domain, statistics are made for all the speckles in a pattern of 600×960 pixels; (b) temporal domain, statistics are made for a certain pixel with 30,000 shots. Two kinds of pseudo-natural light models with uniform distribution and Bernoulli distribution ($p_1 = 0.94$, $c = 0.5$) are discussed in comparison with standard Rayleigh statistics.
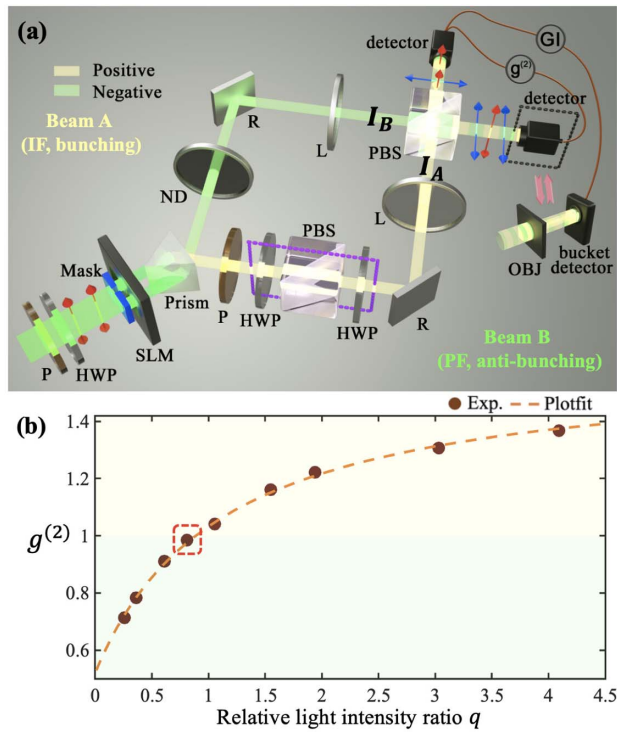
Fig. 12. Experimental details of polarization-sensitive GI. (a) Experimental setup of second-order correlation coefficient measurement of the hybrid illumination and the polarization-sensitive GI. P, polarizer; R, reflector; ND, neutral density filter; HWP, half-wave plate; L, imaging lens; OBJ, object; the three optical elements (HWP-PBS-HWP) in the purple dotted box can continuously adjust the intensity and set the polarization angle of the IF source to be oriented at 45°. (b) Tunable correlation of the hybrid illumination with the change of the relative intensity ratio q, and the curve is fitted according to Eq. (A1). The polarization-sensitive GI experiment in the primary experiment is conducted at the condition of $g^{(2)} \approx 1$, which is highlighted with the red dashed box in (b).

I_A and I_B are intensities of two independent light sources A and B with IF and PF, respectively. The correlations of the two light fields are completely opposite: one (beam B) does not pass through a polarizer and exhibits the antibunching effect due to PF, while the other (beam A) passes through a polarizer, and PF degenerates into IF with a fixed polarization angle of 45°. Note that the two fluctuations driven by different areas of the SLM are statistically independent, and the uniform distribution is applied. In this case, as shown in Fig. 12(b), the second-order cross-correlation coefficient of this hybrid illumination is also tunable compared to Fig. 2 by adjusting the relative intensity q of two beams. In the polarization-sensitive GI experiment, notably, we adjust the relative intensity q of two beams to make $g^{(2)} \approx 1$. At this time, however, it seems common sense that GI can be implemented only if $g^{(2)}_{I_x I_y} \neq 1$. This view is indeed correct, but only for an ordinary transmissive object, but it is wrong for any polarization-sensitive objects in our system with both PF and IF.

In almost all imaging modalities, to obtain a polarization-sensitive image, one must collect the two images of two mutually orthogonal components, and then complete the dif-

ferential operation in the postprocessing. However, in our GI modality, by multiplexing bunching and antibunching into two orthogonal polarization components, only a single round of acquisition is required, and no subsequent differential operations are needed. It is an interesting and special feature that only occurs in GI modality using the hybrid illumination. Also, the edge-enhanced GI experiment presented in Fig. 7 has similar advantages.

4. Definition of CNR
For an imaging signal $G(x)$, CNR is defined as

$$C_{NR} = \frac{|\langle G(x_{in}) \rangle - \langle G(x_{out}) \rangle|}{\Delta G(x_{in}) + \Delta G(x_{out})}, \quad \text{(A2)}$$

where x_{in} and x_{out} denote the pixel positions of in-object and out-object, respectively. To evaluate both positive and negative ghost images in a fair way, note that an absolute value operation is applied. The variance $[\Delta G(x)]^2$ is given by

$$[\Delta G(x)]^2 = \langle [G(x)]^2 \rangle - \langle G(x) \rangle^2. \quad \text{(A3)}$$

Disclosures. The authors declare no conflicts of interest.

Data Availability. Data underlying the results presented in this paper are not publicly available at this time but may be obtained from the authors upon reasonable request.

REFERENCES

1. R. H. Brown and R. Q. Twiss, "Correlation between photons in two coherent beams of light," Nature **177**, 27–29 (1956).
2. R. H. Brown and R. Q. Twiss, "A test of a new type of stellar interferometer on Sirius," Nature **178**, 1046–1048 (1956).
3. R. S. Bennink, S. J. Bentley, and R. W. Boyd, "'Two-photon' coincidence imaging with a classical source," Phys. Rev. Lett. **89**, 113601 (2002).
4. R. S. Bennink, S. J. Bentley, R. W. Boyd, and J. C. Howell, "Quantum and classical coincidence imaging," Phys. Rev. Lett. **92**, 033601 (2004).
5. A. Gatti, E. Brambilla, M. Bache, and L. A. Lugiato, "Ghost imaging with thermal light: comparing entanglement and classical correlation," Phys. Rev. Lett. **93**, 093602 (2004).
6. Y. Cai and S. Y. Zhu, "Ghost interference with partially coherent radiation," Opt. Lett. **29**, 2716–2718 (2004).
7. K. Wang and D. Z. Cao, "Subwavelength coincidence interference with classical thermal light," Phys. Rev. A **70**, 041801 (2004).
8. J. Cheng and S. Han, "Incoherent coincidence imaging and its applicability in X-ray diffraction," Phys. Rev. Lett. **92**, 093903 (2004).
9. D. Z. Cao, J. Xiong, and K. Wang, "Geometrical optics in correlated imaging systems," Phys. Rev. A **71**, 013801 (2005).
10. F. Ferri, D. Magatti, A. Gatti, M. Bache, E. Brambilla, and L. A. Lugiato, "High-resolution ghost image and ghost diffraction experiments with thermal light," Phys. Rev. Lett. **94**, 183602 (2005).
11. A. Valencia, G. Scarcelli, M. D'Angelo, and Y. Shih, "Two-photon imaging with thermal light," Phys. Rev. Lett. **94**, 063601 (2005).
12. J. Xiong, D. Z. Cao, F. Huang, H. G. Li, X. J. Sun, and K. Wang, "Experimental observation of classical subwavelength interference with a pseudothermal light source," Phys. Rev. Lett. **94**, 173601 (2005).

13. D. Zhang, Y. H. Zhai, L. A. Wu, and X. H. Chen, "Correlated two-photon imaging with true thermal light," Opt. Lett. **30**, 2354–2356 (2005).

14. D. Z. Cao, J. Xiong, S. H. Zhang, L. F. Lin, L. Gao, and K. Wang, "Enhancing visibility and resolution in *N*th-order intensity correlation of thermal light," Appl. Phys. Lett. **92**, 201102 (2008).

15. J. H. Shapiro, "Computational ghost imaging," Phys. Rev. A **78**, 061802 (2008).

16. F. T. Arecchi, "Measurement of the statistical distribution of Gaussian and laser sources," Phys. Rev. Lett. **15**, 912–916 (1965).

17. R. C. Liu, B. Odom, Y. Yamamoto, and S. Tarucha, "Quantum interference in electron collision," Nature **391**, 263–265 (1998).

18. M. Henny, S. Oberholzer, C. Strunk, T. Heinzel, K. Ensslin, M. Holland, and C. Schönenberger, "The fermionic Hanbury Brown and Twiss experiment," Science **284**, 296–298 (1999).

19. H. Kiesel, A. Renz, and F. Hasselbach, "Observation of Hanbury Brown-Twiss anticorrelations for free electrons," Nature **418**, 392–394 (2002).

20. S. Gan, D. Z. Cao, and K. Wang, "Dark quantum imaging with fermions," Phys. Rev. A **80**, 043809 (2009).

21. H. J. Kimble, M. Dagenais, and L. Mandel, "Photon antibunching in resonance fluorescence," Phys. Rev. Lett. **39**, 691–695 (1977).

22. P. Michler, A. Imamoglu, M. D. Mason, P. J. Carson, G. F. Strouse, and S. K. Buratto, "Quantum correlation among photons from a single quantum dot at room temperature," Nature **406**, 968–970 (2000).

23. R. Boddeda, Q. Glorieux, A. Bramati, and S. Pigeon, "Generating strong anti-bunching by interfering nonclassical and classical states of light," J. Phys. B **52**, 215401 (2019).

24. I. Starshynov, A. M. Paniagua-Diaz, N. Fayard, A. Goetschy, R. Pierrat, R. Carminati, and J. Bertolotti, "Non-Gaussian correlations between reflected and transmitted intensity patterns emerging from opaque disordered media," Phys. Rev. X **8**, 021041 (2018).

25. A. M. Paniagua-Diaz, I. Starshynov, N. Fayard, A. Goetschy, R. Pierrat, R. Carminati, and J. Bertolotti, "Blind ghost imaging," Optica **6**, 460–464 (2019).

26. T. Grujic, S. R. Clark, D. Jaksch, and D. G. Angelakis, "Repulsively induced photon superbunching in driven resonator arrays," Phys. Rev. A **87**, 053846 (2013).

27. Z. Ficek, "Highly directional photon superbunching from a few-atom chain of emitters," Phys. Rev. A **98**, 063824 (2018).

28. M. Marconi, J. Javaloyes, P. Hamel, F. Raineri, A. Levenson, and A. M. Yacomotti, "Far-from-equilibrium route to superthermal light in bimodal nanolasers," Phys. Rev. X **8**, 011013 (2018).

29. C. C. Leon, A. Rosławska, A. Grewal, O. Gunnarsson, K. Kuhnke, and K. Kern, "Photon superbunching from a generic tunnel junction," Sci. Adv. **5**, eaav4986 (2019).

30. Y. Zhou, F. L. Li, B. Bai, H. Chen, J. Liu, Z. Xu, and H. Zheng, "Superbunching pseudothermal light," Phys. Rev. A **95**, 053809 (2017).

31. L. Zhang, Y. Lu, D. Zhou, H. Zhang, L. Li, and G. Zhang, "Superbunching effect of classical light with a digitally designed spatially phase-correlated wave front," Phys. Rev. A **99**, 063827 (2019).

32. F. Gori and M. Santarsiero, "Spatial superbunching of light: model sources," Opt. Lett. **44**, 4012–4015 (2019).

33. N. Bender, H. Yılmaz, Y. Bromberg, and H. Cao, "Creating and controlling complex light," APL Photonics **4**, 110806 (2019).

34. A. Roy and M. M. Brundavanam, "Polarization-based intensity correlation of a depolarized speckle pattern," Opt. Lett. **46**, 4896–4899 (2021).

35. C. Q. Wei, J. B. Liu, X. X. Zhang, R. Zhuang, Y. Zhou, H. Chen, Y. C. He, H. B. Zheng, and Z. Xu, "Non-Rayleigh photon statistics of super-bunching pseudothermal light," Chin. Phys. B **31**, 024209 (2022).

36. I. Straka, J. Mika, and M. Ježek, "Generator of arbitrary classical photon statistics," Opt. Express **26**, 8998–9010 (2018).

37. M. Blazek and W. Elsäßer, "Coherent and thermal light: tunable hybrid states with second-order coherence without first-order coherence," Phys. Rev. A **84**, 063840 (2011).

38. H. E. Kondakci, A. Szameit, A. F. Abouraddy, D. N. Christodoulides, and B. E. A. Saleh, "Sub-thermal to super-thermal light statistics from a disordered lattice via deterministic control of excitation symmetry," Optica **3**, 477–482 (2016).

39. S. Zhang, H. Zheng, G. Wang, J. Liu, S. Luo, Y. He, Y. Zhou, H. Chen, and Z. Xu, "Controllable superbunching effect from four-wave mixing process in atomic vapor," Opt. Express **28**, 21489–21498 (2020).

40. X. F. Liu, X. H. Chen, X. R. Yao, W. K. Yu, G. J. Zhai, and L. A. Wu, "Lensless ghost imaging with sunlight," Opt. Lett. **39**, 2314–2317 (2014).

41. A. Shevchenko, T. Setälä, M. Kaivola, and A. T. Friberg, "Characterization of polarization fluctuations in random electromagnetic beams," New J. Phys. **11**, 073004 (2009).

42. T. Shirai and E. Wolf, "Correlations between intensity fluctuations in stochastic electromagnetic beams of any state of coherence and polarization," Opt. Commun. **272**, 289–292 (2007).

43. X. Liu, G. Wu, X. Pang, D. Kuebel, and T. D. Visser, "Polarization and coherence in the Hanbury Brown-Twiss effect," J. Mod. Opt. **65**, 1437–1441 (2018).

44. D. Kuebel and T. D. Visser, "Generalized Hanbury Brown-Twiss effect for Stokes parameters," J. Opt. Soc. Am. A **36**, 362–367 (2019).

45. G. Wu, D. Kuebel, and T. D. Visser, "Generalized Hanbury Brown-Twiss effect in partially coherent electromagnetic beams," Phys. Rev. A **99**, 033846 (2019).

46. O. Korotkova and Y. Ata, "Electromagnetic Hanbury Brown and Twiss effect in atmospheric turbulence," Photonics **8**, 186 (2021).

47. C. Maurer, A. Jesacher, S. Fürhapter, S. Bernet, and M. Ritsch-Marte, "Tailoring of arbitrary optical vector beams," New J. Phys. **9**, 78 (2007).

48. D. Preece, S. Keen, E. Botvinick, R. Bowman, M. Padgett, and J. Leach, "Independent polarisation control of multiple optical traps," Opt. Express **16**, 15897–15902 (2008).

49. A. Shevchenko, M. Roussey, A. T. Friberg, and T. Setälä, "Polarization time of unpolarized light," Optica **4**, 64–70 (2017).

50. M. Born and E. Wolf, *Principles of Optics*, 7th expanded ed. (Cambridge University, 1999), p. 32.

51. K. W. C. Chan, M. N. O'Sullivan, and R. W. Boyd, "High-order thermal ghost imaging," Opt. Lett. **34**, 3343–3345 (2009).

52. M. P. Rowe, E. N. Pugh, J. S. Tyo, and N. Engheta, "Polarization-difference imaging: a biologically inspired technique for observation through scattering media," Opt. Lett. **20**, 608–610 (1995).

53. H. Defienne, B. Ndagano, A. Lyons, and D. Faccio, "Polarization entanglement-enabled quantum holography," Nat. Phys. **17**, 591–597 (2021).

54. E. E. Gorodnichev, A. I. Kuzovlev, and D. B. Rogozkin, "Impact of wave polarization on long-range intensity correlations in a disordered medium," J. Opt. Soc. Am. A **33**, 95–106 (2016).

55. Z. Jiang, Z. Wang, K. Cheng, and T. Wang, "Correlation between intensity fluctuations and degree of cross-polarization of light waves on scattering," Optik **198**, 163308 (2019).